

A tunable acoustic metasurface via one-dimensional mechanical adjustment for real-time focusing

Jie Hu(胡洁), Mengqi Jiang(姜梦琦), Rui Zang(藏瑞), and Yuhang Qian(钱宇航)
Citation: Chin. Phys. B, 2025, 34 (**10**): 104301. DOI: 10.1088/1674-1056/add7ac
http://cpb.iphy.ac.cn; http://iopscience.iop.org/cpb

What follows is a list of articles you may be interested in

Computation and analysis of the characteristic spectra of Eu(II) ions in single-bubble sonoluminescence

Xue-Ping Wang(王学坪) and Jin-Fu Liang(梁金福)
Chin. Phys. B, 2025, 34 (**9**): 094301. DOI: 10.1088/1674-1056/addaa1

Effect of metal plate on ultrasonic cavitation field distribution

Jin-He Liu(刘金河), Zhuang-Zhi Shen(沈壮志), Peng-Fei Cao(曹鹏飞), Jian-Feng Li(李建锋), and Xiao-Qiang Bai(白小强)
Chin. Phys. B, 2025, 34 (**5**): 054302. DOI: 10.1088/1674-1056/adca9d

Overcoming bandwidth limitations in space-coiled acoustic metamaterials through inclined perforated plate design

Jixin Liu(刘继鑫), Fengmin Wu(吴丰民), Ting Li(李婷), Junjun Wang(王军军), Xinye Zou(邹欣晔), and Dong Zhang(章东)
Chin. Phys. B, 2025, 34 (**1**): 014303. DOI: 10.1088/1674-1056/ad8fa2

Lamb wave TDTE super-resolution imaging assisted by deep learning

Liu-Jia Sun(孙刘家), Qing-Bang Han(韩庆邦), and Qi-Lin Jin(靳琪琳)
Chin. Phys. B, 2025, 34 (**1**): 014301. DOI: 10.1088/1674-1056/ad886d

Acoustic radiation force on a cylindrical composite particle with an elastic thin shell and an internal eccentric liquid column in a plane ultrasonic wave field

Rui-Qi Pan(潘瑞琪), Zhi-Wei Du(杜芷玮), Cheng-Hui Wang(王成会), Jing Hu(胡静), and Run-Yang Mo(莫润阳)
Chin. Phys. B, 2024, 33 (**9**): 094302. DOI: 10.1088/1674-1056/ad5d66

A tunable acoustic metasurface via one-dimensional mechanical adjustment for real-time focusing

Jie Hu(胡洁)[†], Mengqi Jiang(姜梦琦), Rui Zang(藏瑞), and Yuhang Qian(钱宇航)

College of Information Science and Technology and College of Artificial Intelligence, Nanjing Forestry University, Nanjing 210000, *China*

(Received 1 April 2025; revised manuscript received 6 May 2025; accepted manuscript online 13 May 2025)

Adjustable or programmable metamaterials offer versatile functions, while the complex multi-dimensional regulation increases workload, and hinders their applications in practical scenarios. To address these challenges, we present a mechanically programmable acoustic metamaterial for real-time focal tuning via one-dimensional phase-gradient modulation in this paper. The device integrates a phase gradient structure with concave cavity channels and an x-shaped telescopic mechanical framework, enabling dynamic adjustment of inter-unit spacing (1 mm–3 mm) through a microcontroller-driven motor. By modulating the spacing between adjacent channels, the phase gradient is precisely controlled, allowing continuous focal shift from 50 mm to 300 mm along the x-axis at 7500 Hz. Broadband focusing is also discussed in the range 6800 Hz–8100 Hz, with transmission coefficients exceeding 0.5, ensuring high efficiency and robust performance. Experimental results align closely with simulations, validating the design's effectiveness and adaptability. Unlike conventional programmable metamaterials requiring multi-dimensional parameter optimization, this approach simplifies real-time control through single-axis mechanical adjustment, significantly reducing operational complexity. Due to the advantages of broadband focusing, simple control mode, real-time monitoring, and so on, the device may have extensive applications in the fields of acoustic imaging, nondestructive testing, ultrasound medical treatment, etc.

Keywords: phase gradient structure, one-dimensional mechanical adjustment, adjustable focusing

PACS: 43.35.+d

DOI: 10.1088/1674-1056/add7ac **CSTR:** 32038.14.CPB.add7ac

1. Introduction

Acoustic focusing has received extensive attention because of its extensive application in sound imaging,[1,2] medical therapy,[3–5] etc. With the development of metamaterials, the mechanisms for realizing acoustic focusing become more diversified, such as adjusting the shape or refractive index of tailored designs,[6–9] regulating the acoustic waves for achieving super-resolution focusing,[10–14] utilizing phase gradient metamaterials based on the generalized Snell's law,[15–18] and so on. However, the passive nature of existing metamaterials produces fixed functionality and narrow bandwidth once fabricated, which can hardly satisfy the versatile requirements of practical applications to remold the produced sound field such as acoustic therapy and imaging.

The emergence of programmable metamaterials has received significant attention due to their enhanced versatility which is lacking in conventional passive metamaterials.[19–23] Mechanical tunability is one of the most common ways to realize tunable acoustic manipulation whose mechanism is to utilize the mechanical reconfigurability of the unit cell itself, like varying the tunable acoustic channel length, cavity size, or resonant characteristics, to achieve flexibility of the metasurface. Zhao *et al*. designed an adjustable spiral folding structure to change the length of the acoustic wave propagation channel by changing the rotary screw depth of the spiral structure.[24] Tian proposed a tunable hybrid resonance unit cell, where the cavity size of the Helmholtz resonator is altered by filling it with water. This enabled a programmable metasurface with various wave manipulation functions.[25] Zhai *et al*. proposed two-dimensional (2D) reflective tunable acoustic metasurfaces which could achieve anomalous reflection as well as focusing function.[26,27] Zhou *et al*. presented a bending channel which can be dynamically adjusted by rotating the angle of the internal rotor.[28] Chen designed a metasurface consisting of Helmholtz resonators with movable sliders and by adjusting the position of the slider, the cavity size can be tuned, enabling full-period phase shifts over a wide frequency band while maintaining high transmission.[29] However, existing acoustic programmable metamaterials typically necessitate manual optimization of individual unit cells, involving multi-dimensional parameter adjustments (e.g., geometry, material composition, and spatial alignment). This iterative process significantly increases computational and experimental workloads and decreases the operating efficiency, thereby limiting real-time adaptability and scalability in practical implementations.

In this paper, we address the need for simple manipulation, high efficiency and real-time flexible design. Therefore, we demonstrate a mechanically reconfigurable metasurface that enables dynamic acoustic control through single-axis

[†]Corresponding author. E-mail: hujie@njfu.edu.cn

© 2025 Chinese Physical Society and IOP Publishing Ltd. All rights, including for text and data mining, AI training, and similar technologies, are reserved.

modulation of inter-unit spacing. The units are fixed on an "x" shaped adjustable telescopic mechanical structure and by driving the electric motor, the retractable mechanical bracket stretches or retracts in one dimension to adjust the distance between the adjacent units. The movement of the metamaterial units induces the change of phase gradient and enables tunability of the focus position. With the interval of units ranging from 1 mm to 3 mm, the focal point shifts from 50 mm to 300 mm along the x-axis. This approach eliminates the need for multi-dimensional parameter recalibration and achieves broadband focusing performance across 6800 Hz–8100 Hz as well. Experimental results closely align with simulations, validating the effectiveness of the device. This approach holds promise for several critical and challenging applications, such as acoustic imaging and directional transmission.

2. Acoustic focusing phase regulation

In this study, we employ a series of concave cavity channels to create a gradient phase structure, with each channel differing in the width of air grooves. The planform schematic of the structure is illustrated in Fig. 1, where the blue region represents the gradient phase structure, and the white region denotes air. The sound speed and density of air are 343 m/s and 1.21 kg/m^3, and this structure employs epoxy resin as the material of choice, which has a sound speed of 2720 m/s and a density of 1180 kg/m^3 and can be considered as acoustically rigid due to the huge contrast between the acoustic impedances of solid and air. As depicted in the lower right side of Fig. 1 which is surrounded by the black dotted box, the concave unit consists of three rectangular air cavities separated by two pink dotted lines. The relevant parameters are $w_1 = 8$ mm, $w_2 = 2$ mm, $w_3 = 10$ mm, $D = 30$ mm. The total length of these cavities is fixed at D, with the left and right cavities being identical, each having a length d_1 and width w_1. In our design, the mechanism of metasurface does not rely on resonance and is thus capable of engineering the incident sound wave with different frequencies. According to the transfer matrix method, by varying the length d_1 within the air groove, the output phase of the air channel is changed. Furthermore, by carefully arranging the d_1 of each unit, a specific phase gradient can be generated between adjacent channels, enabling phase regulation.

The variation in d_1 not only affects the output phase of each channel but also induces changes in amplitude which influence the focusing performance. When d_1/D ranges from 0.13 to 0.21, the transmission coefficient exhibits a frequency-dependent behavior, as illustrated in Fig. 2. The transmission coefficient is quantitatively defined as the ratio of the transmitted wave's acoustic intensity to that of the incident wave, following the conventional definition in acoustic wave theory. From the figure, it can be observed that the transmission coefficient generally exceeds 0.5 within the frequency range of 6800 Hz to 8100 Hz for channels of varying sizes. This high transmission is crucial for ensuring effective focusing, as the intensity of the transmitted waves directly influences the quality and intensity of the resulting focus. Therefore, to achieve optimal focusing, it is essential that the transmission coefficient remains above 0.5 within the operational frequency range.

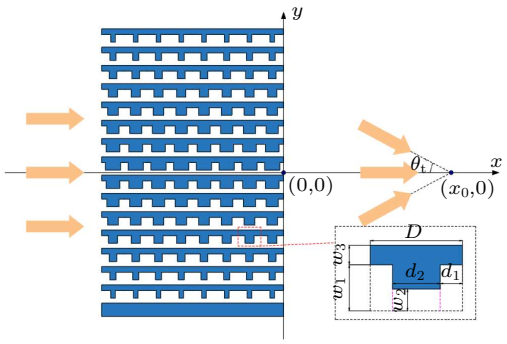


Fig. 1. Structural block diagram of phase gradient structure, the white part is the air channel, the blue part is the rigid material.

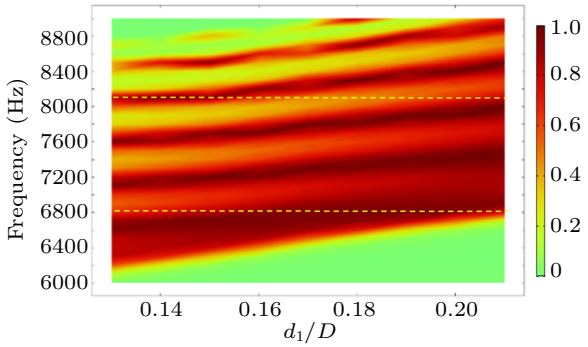


Fig. 2. Transmittance varies with frequency when the ratio d_1/D ranges from 0.13 to 0.21.

To further investigate the focusing capabilities of the structure, we select 7500 Hz as an example, as it lies within the frequency range where the transmission coefficient consistently exceeds 0.5, ensuring robust and reliable focusing performance.

Here we define the central position on the right edge of the entire structure as (0,0) when the incident plane acoustic waves propagate from the left side, as shown in Fig. 1. Therefore, to focus the acoustic waves at the point (x_0, 0), the transmission angle θ_t of the incident waves should satisfy

$$\sin\theta_t = \frac{|y|}{\sqrt{y^2 + x_0^2}}. \tag{1}$$

Based on Eq. (1) and the generalized Snell's law,[30] the phase shift in the y-axis is

$$\phi(y) = k_0 \left[\sqrt{y^2 + x_0^2} - x_0 \right], \tag{2}$$

where $k_0 = 2\pi/\lambda$ is the wave number, and λ is the wavelength in air.

Taking the incident acoustic frequency of 7500 Hz and the preset focal length $x_0 = 200$ mm as an example, the phase distribution along the y-axis is illustrated in Fig. 3(a). Subsequently, we systematically calculate the phase shift for each unit across different d_1/D values at $w_2 = 2$ mm, as shown in Fig. 3(b).

It is evident that to achieve the desired phase distribution, the d_1/D distribution has to be symmetrical in the vertical direction. Based on these findings, the entire structure is designed accordingly. If 8 units are chosen in the upper and lower sides, respectively, the arrangement of units in the gradient structure at 7500 Hz is presented in Fig. 3(c), demonstrating how the phase distribution and phase shift calculations inform the structure design.

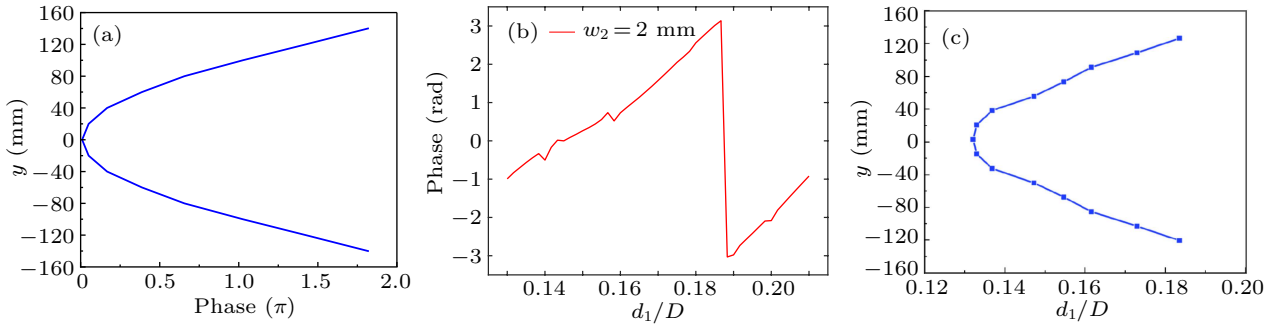


Fig. 3. (a) Phase distribution along the y-axis when focusing at (200,0) at 7500 Hz, (b) the phase shift as a function of d_1/D at $w_2 = 2$ mm, (c) the position of each unit along y-axis as a function of d_1/D.

Modulating the ratio d_1/D of the cell structure enables the phase gradient configuration and focusing of the acoustic waves. However, the focusing position remains fixed at a single frequency of acoustic incidence, which significantly limits the practical applicability of the structure. To address this limitation, we propose a method to control the phase gradient by dynamically adjusting the interval w_2 between adjacent units. This approach allows for the tunability of the focal position, thereby enhancing the versatility and functionality of the structure.

As shown in Fig. 4(a), the structures achieve full 2π phase coverage at 7500 Hz when the ratio d_1/D varies from 0.14 to 0.2, with w_2 values of 1 mm and 2 mm. And the phase gradient for $w_2 = 1$ mm is significantly larger than that for $w_2 = 2$ mm. That can be explained by defining the difference of phase shift of adjacent units as $\Delta\varphi$ and L representing their spacing, then the phase gradient can be expressed as $\Delta\varphi/L$. Notably, an increase in L directly reduces the phase gradient $\Delta\varphi/L$. This relationship explains the steeper slope observed in the $w_2 = 1$ mm curve compared to the $w_2 = 2$ mm curve in Fig. 4(a). Consequently, adjusting the spacing between air channels alters the phase gradient, thereby inducing a shift in the focal position.

Figure 4(a) demonstrates that increasing w_2 reduces the phase gradient, which in turn diminishes the wave deflection angle and elongates the focal point along the x-axis. Figure 4(b) further quantifies the shift in focal position as w_2 varies from 1 mm to 3 mm under the d_1/D configuration defined in Fig. 3(c). The focal length exhibits an approximately linear dependence on w_2, indicating that the focal point systematically shifts away from the structure as w_2 increases.

These findings confirm that once the d_1/D configuration of each unit is determined, the phase gradient, although modulated by w_2, does not affect the focal behavior. However, as w_2 increases, the focal position progressively shifts further from the structure.

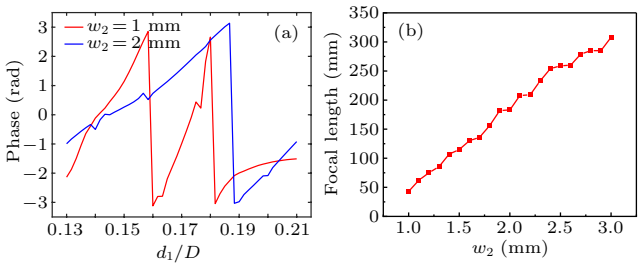


Fig. 4. (a) Phase change with the ratio d_1/D at 7500 Hz, the red and blue line corresponding to $w_2 = 1$ mm, and 2 mm, respectively. (b) Schematic diagram of focus position when the interval w_2 increases.

3. Adjustable mechanical structure and experimental device

To assess the effectiveness of the proposed mechanism, we performed simulations using the finite element method and conducted experiments with a telescopic mechanical structure. 16 units are employed and the ratio d_1/D of each air channel is aligned symmetrically as Fig. 3(c).

A focus-controllable device based on an x-type adjustable mechanical structure is designed as illustrated in Fig. 5(a), with the right side and upward views of the mechanical structure shown in Figs. 5(b) and 5(c), respectively. The entire structure consists of three layers, and the middle layer contains sliders with the same number as the gradient units of the metasurface, acting as carriers that connect the bottom x-shape

connecting rods to the top gradient units. The sliders are traversed by three poles in x direction: the center motor-driven screw ensures the movement of the whole structure, while two smooth poles on either side provide support (Fig. 5(b)). When the motor works, the screw starts rotating to drive the slides extending or retracting along x-axis, except for the leftmost slider, which remains fixed to the immobile substrate (Fig. 5(c)). The bottom layer features x-shape connecting rods, with uniform and adjustable spacing between each rod. The top layer consists of units of metasurface affixed to movable sliders, enabling phase gradient autofocus through the extension or retraction of the sliders. In the design, the speed and timing of the screw rotation can be adjusted programmatically, allowing all units to move synchronously to the left or right along x-axis in real-time, with the exception of the leftmost unit, which remains fixed.

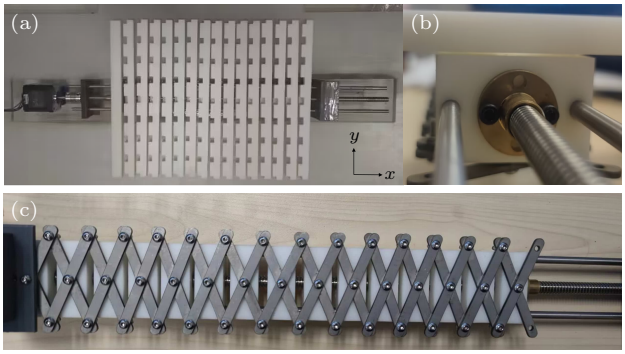


Fig. 5. (a) Photograph of integral structure of focus controllable device (including motor), (b) the right view of the adjustable mechanical structure, (c) the bottom of the adjustable mechanical structure.

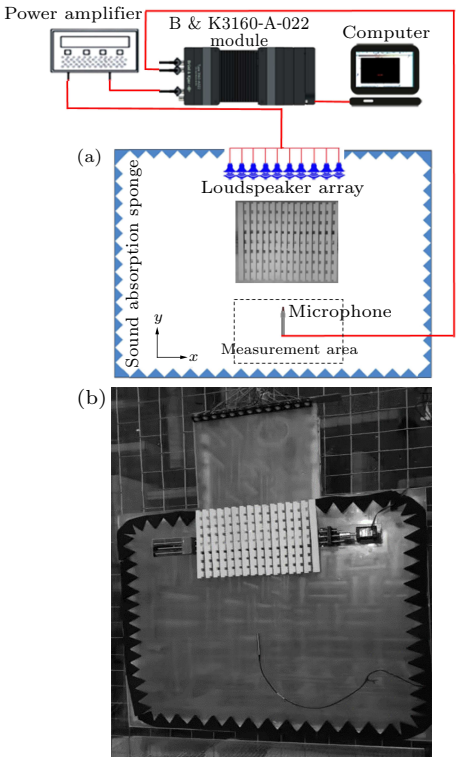


Fig. 6. (a) Diagram of the experimental design, (b) photograph of the experimental scene.

The experimental diagram is illustrated in Fig. 6(a), where the metasurface structure is positioned within a planar waveguide, clamped by two parallel acrylic plates. The sound-absorbing sponge at the boundary of the waveguide minimizes the reflection of waves from the waveguide into free space. The loudspeaker array, powered by an amplifier, generates incident plane waves, while a microphone is utilized to measure the sound pressure of the transmitted acoustic waves.

The experiment is conducted in an anechoic chamber, as shown in Fig. 6(b). The two parallel acrylic plates are elevated to provide enough space for the actuating device, which connects to the metasurface via a hole in the lower plate, enabling real-time focusing control. A stepper motor (42BYG48) is employed in the adjustable mechanical device which is driven by a motor driver TB6600 controlled by a microcontroller STM32. The experimental data is recorded by the microphone Brüel & Kjær 3160-A-022.

4. Adjustable focusing

By programmatically controlling the x-type mechanical structure, the spacing between each unit is dynamically adjusted, enabling tunable phase gradients and focal position shifts. Here we investigate the effectiveness of the metasurface with three distinct values of w_2: 1 mm, 2 mm, and 3 mm, respectively. Acoustic waves passing through the structure focus at positions closely matching the preset focal coordinates (Fig. 4(b)). The simulated and experimental sound pressure distributions in the transmitted field are shown in Figs. 7(a1)–7(a3). The measured focusing position with a yellow cross sign is marked in the simulated acoustic field which demonstrates that our designed focusing adjustable metasurface precisely converges the incident acoustic energy into the expected focal region. Notably, the focal point shifts rightward along the x-axis as w_2 increases. While simulated and experimental focal positions align spatially, the experimental focal beams exhibit striped interference patterns in the pressure distribution (particularly in Figs. 7(a2) and 7(a_3)), attributed to reflections during experiments.

Figures 7(b1)–7(b3) display the normalized sound pressure profiles along the x-axis centered at the focal point. Due to the size limitation of the parallel waveguide in the experiment setup, only 9 points near the focus are measured. Despite this constraint, the overall trend of the experimental results is substantially consistent with the simulation results. For $w_2 = 1$ mm, the simulated pressure maximum at $x =$ 43 mm, whereas the experimental peak shifts to $x = 50$ mm. When $w_2 = 2$ mm, the theoretical focal position at (200,0) aligns closely with the experimental pressure maximum in Fig. 7(b_2). Similarly, the agreement between simulation and experiment is observed for $w_2 = 3$ (Fig. 7(b3)). The deviation

between simulation and experiment arises from minor fabrication inaccuracies in the metasurface, and mechanical tolerances in spacing control, particularly at smaller scales (e.g., $w_2 = 1$ mm).

The y-axis sound pressure profiles (Figs. 7(c1)–7(c3)) further confirm consistency in trends between experiments and simulations. However, deviations in experimental data — attributed to fabrication imperfections and motor control limitations — become more evident at reduced spatial scales. In addition, the full width at half maximum (FWHM) exhibits a pronounced dependence on the structural parameter w_2, with values of 0.39λ, 0.79λ, and 1.14λ corresponding to $w_2 = 1$ mm, 2 mm, and 3 mm, respectively. These results demonstrate a statistically significant inverse correlation between w_2 and focusing resolution, with subwavelength focusing ($< 0.5\lambda$) achieved at $w_2 = 1$ mm.

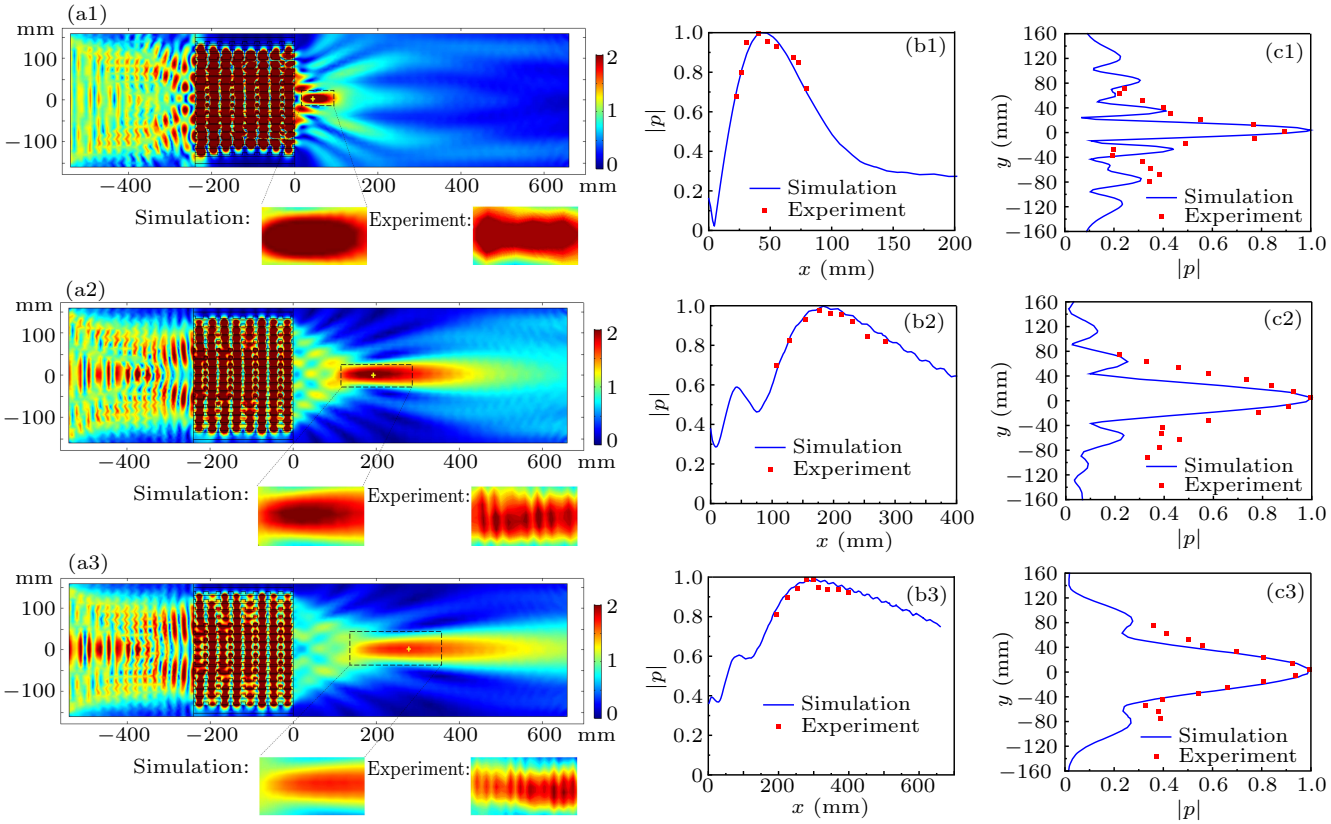


Fig. 7. Sound pressure distribution when frequency is 7500 Hz and interval w_2 is 1 mm–3 mm: (a1)–(a3) sound pressure diagram with $w_2 = 1$ mm, 2 mm, 3 mm respectively. (b1)–(b3) Normalized sound pressure along x axis at focal point with $w_2 = 1$ mm, 2 mm, 3 mm respectively. (c1)–(c3) Normalized sound pressure along y axis at focal point with $w_2 = 1$ mm, 2 mm, 3 mm respectively.

Therefore, precise presetting of the structural parameter d_1/D and controlled adjustment of inter-unit spacing enables alignment of the phase requirements across unit cells, theoretically allowing focal positioning at arbitrary locations within the transmitted field. Both simulations and experiments validate the efficacy of the proposed metasurface. Observed discrepancies between simulated and experimental results stem from fabrication inaccuracies of the gradient-index metasurface and mechanical tolerances in the single-axis motor system governing w_2 adjustments.

Unlike conventional programmable metamaterial designs that rely on multi-dimensional parameter tuning, our approach employs a programmatically controlled screw mechanism to dynamically adjust the spacing w_2 along a single axis. This simplified one-dimensional mechanical system achieves tunable focusing while minimizing design complexity.

5. Broadband characteristics of acoustic focusing

As demonstrated above, tuning the structural ratio d_1/D within the range of 0.13–0.21 enables effective acoustic focusing across a broad frequency spectrum (6800 Hz–8100 Hz). To validate the metasurface's broadband performance, simulations and experiments are conducted at the frequency of 7000 Hz and 8000 Hz, with w_2 fixed at 2 mm. The simulated and experimental results are shown in Fig. 8.

Figures 8(a) and 8(b) depict the simulated and experimental sound pressure distributions at 7000 Hz and 8000 Hz, respectively, demonstrating the metasurface's robust broadband focusing capability. Consistent with observations at 7500 Hz (Fig. 7), reflections of acoustic waves propagate into the measurement zone and superimpose with the focal field, generating pronounced interference fringes in the pressure profiles

and these artifacts arise from constructive and destructive interference between the incident and reflected wavefronts.

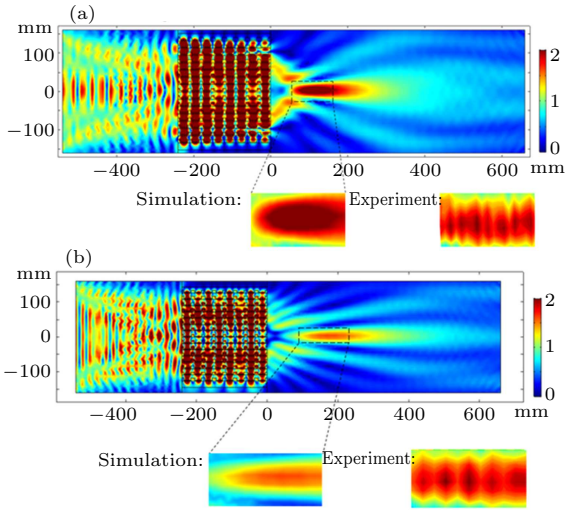


Fig. 8. Sound pressure distribution with different incident frequencies 7000 Hz (a) and 8000 Hz (b) respectively.

6. Conclusion

In summary, we present a mechanically reconfigurable acoustic metasurface for real-time focal tuning via one-dimensional phase-gradient engineering. By dynamically adjusting the inter-channel spacing w_2 through a programmable mechanical system, phase gradient modulation is achieved, enabling continuous focal shifts along the x-axis without requiring individual unit-level recalibration. The phase gradient shift caused by programming the mechanic device results in a corresponding shift in the focal point along the x-axis. Experimental and simulation results exhibit strong agreement across 7000 Hz–8000 Hz, validating the structure's broadband programmability. The adjustable acoustic focusing mechanism presented in this paper is easily fabricated in real-time control, suggesting potential applications in medical diagnosis, acoustic imaging, nondestructive testing, etc.

Acknowledgement

Project supported by the National Natural Science Foundation of China (Grant No. 12374416).

References

[1] Chan V and Perlas A 2011 *Basics of Ultrasound Imaging* (New York: Springer)
[2] Gholampour A, Sakhaei S M and Andargoli S M H 2017 *Ultrasonics* **76** 10
[3] Harary M, Segar D J, Huang K T, Tafel I J, Valdes P A and Cosgrove G R 2018 *Neurosurgical Focus FOC* **44** E2
[4] Darrow D P 2019 *Neurotherapeutics* **16** 88
[5] Collins K, Brocken E, Bahler C D, Alabd A, Koch M O and Cheng L 2022 *Human Pathology* **119** 79
[6] Lin S C, Tittmann B R and Huang T J 2012 *J. Appl. Phys.* **111** 123510
[7] Celli P and Gonella S 2014 *J. Appl. Phys.* **115** 103502
[8] Alagoz S, Alagoz B B, Sahin A and Nur S 2015 *Chin. Phys. B* **24** 046201
[9] Han M L, Tang R Y, Ma N, Zhang G B and Zhang X F 2025 *Chin. Phys. B* **34** 40702
[10] Ambati M, Fang N, Sun C and Zhang X 2007 *Phys. Rev. B* **75** 195447
[11] Jung J, García-Vidal F J, Martín-Moreno L and Pendry J B 2009 *Phys. Rev. B* **79** 153407
[12] Zhu J, Christensen J, Jung J, Martin-Moreno L, Yin X, Fok L, Zhang X and Garcia-Vidal F J 2011 *Nat. Phys.* **7** 52
[13] Park J J, Park C M, Lee K J B and Lee S H 2015 *Appl. Phys. Lett.* **106** 051901
[14] Sun L J, Han Q B and Jin Q L 2025 *Chin. Phys. B* **34** 14301
[15] Li Y, Jiang X, Li R Q, Liang B, Zou X Y, Yin L L and Cheng J C 2014 *Phys. Rev. Appl.* **2** 064002
[16] Lan J, Li Y, Xu Y and Liu X 2017 *Sci. Rep.* **7** 10587
[17] Zhu X F and Lau S K 2019 *J. Appl. Phys.* **126** 224504
[18] Liang D, Hu G, Ding N, Ma Q, Guo G, Li Y, Tu J and Zhang D 2022 *IEEE Transactions on Ultrasonics, Ferroelectrics and Frequency Control* **69** 377
[19] Popa B I, Zigoneanu L and Cummer S A 2013 *Phys. Rev. B* **88** 024303
[20] Popa B I, Shinde D, Konneker A and Cummer S A 2015 *Phys. Rev. B* **91** 220303
[21] Chen X, Liu P, Hou Z and Pei Y 2017 *Sci. Rep.* **7** 9050
[22] Ma G, Fan X, Sheng P and Fink M 2018 *Proc. Nat. Acad. Sci. USA* **115** 6638
[23] Tang Y F and Lin S Y 2023 *Chin. Phys. B* **32** 034306
[24] Zhao S D, Chen A L, Wang Y S and Zhang C 2018 *Phys. Rev. Appl.* **10** 054066
[25] Tian Z, Shen C, Li J, Reit E, Gu Y, Fu H, Cummer S A and Huang T J 2019 *Adv. Funct. Mater.* **29** 1808489
[26] Zhai S, Song K, Ding C, Wang Y, Dong Y and Zhao X 2018 *Materials* **11** 1976
[27] Wang X L, Yang J, Liang B and Cheng J C 2020 *Appl. Phys. Express* **13** 014002
[28] Zhou H T, Fan S W, Li X S, Fu W X, Wang Y F and Wang Y S 2020 *Smart Materials and Structures* **29** 065016
[29] Chen Z, Shao S, Negahban M and Li Z 2019 *J. Phys. D: Appl. Phys.* **52** 395503
[30] Yu N, Genevet P, Kats M A, Aieta F, Tetienne J P, Capasso F and Gaburro Z 2011 *Science* **334** 333